Biomaterials Science

ROYAL SOCIETY OF CHEMISTRY

PAPER

View Article Online
View Journal | View Issue

Cite this: *Biomater. Sci.*, 2025, **13**, 1075

Biofabricated tissue model for determining biocompatibility of metallic coatings†

Taha Cagri Senocak, [a,b] Pavan Kumar Reddy Gudeti, [b] Joanna Żur-Pińska[b] and Małgorzata Katarzyna Włodarczyk-Biegun *[b,c]

Metallic biomaterials are extensively used in orthopedics and dentistry, either as implants or coatings. In both cases, metal ions come into contact with surrounding tissues causing a particular cell response. Here, we present a biofabricated *in vitro* tissue model, consisting of a hydrogel reinforced with a melt electrowritten mesh, to study the effects of bound and released metal ions on surrounding cells embedded in a hydrogel matrix. We evaluate the biocompatibility, bioactivity, and antibacterial properties of these metal coatings. Our approach involves integrating physical vapour deposition coating technology with 3D bioprinting methods. To produce tissue models, melt electrowritten (MEW) meshes composed of polycaprolactone (PCL) were printed and integrated into cell-laden methacrylated galatin (GelMa). The mouse embryonic fibroblast cell line (NIH3T3) was used. GelMa concentration and printing parameters for MEW were adjusted and mechanical analysis of the models was performed to find the optimal material composition. Optimized models were placed on the glass slide surfaces coated with typically non-toxic metals, *i.e.* titanium (**Ti**), tantalum (**Ta**), zirconium (**Zr**), silver (**Ag**), tungsten (**W**), and niobium (**Nb**). Except for **W**, all other coatings were stable in a physiological wet environment, as studied by SEM. The viability of the cells at different distances from the coated surface was analyzed. Antibacterial tests against pathogens *Staphylococcus aureus* and *Escherichia coli* were used to assess the models' resistance, important for infection control. While **Ag** coatings showed toxicity, **Nb**, **Ta**, **Ti**, and **Zr** coatings promoted fibroblast growth, with the highest cell viability after 14 days of culture revealed for **Ta** and **Nb**. The strongest antimicrobial effect against *E. coli* and *S. aureus* was observed for **Ag** and **W**, while **Ta** exhibited antibacterial activity only against *S. aureus*. From a broader perspective, our work offers an effective 3D *in vitro* model for an in-depth characterization of the biocompatibility of metals and metal coatings.

Received 8th October 2024,
Accepted 4th January 2025

DOI: 10.1039/d4bm01335b

rsc.li/biomaterials-science

1. Introduction

Organ and tissue loss presents substantial health challenges, necessitating innovative solutions to meet the increasing demand for transplantations.[1] Notably, developments in medical implants have revolutionized the treatment of various conditions in dentistry and orthopaedics. Metallic implants, such as dental implants, joint replacements, and bone plates, play a crucial role in these fields.[2] Furthermore, there is a growing interest in integrating soft electronics within tissues, which opens new frontiers for medical applications.[3] Metallic materials for use inside the body must exhibit particular mechanical properties (*e.g.*, high mechanical strength to withstand the stress of chewing or movement), as well as excellent wear and corrosion resistance. Additionally, they need to be biologically compatible to prevent adverse reactions from surrounding tissues.[4–7]

Different metallic bioimplants have been proposed so far, due to their durability, strength, longevity, bioactivity and biocompatibility, corrosion resistance, and aesthetic suitability.[8] For instance, silver's (**Ag**) antibacterial properties make it ideal for wound dressings and catheters,[9–11] while niobium (**Nb**) is used in implant castings due to its corrosion resistance and electrical conductivity.[12–15] Tantalum (**Ta**) finds application in devices like stents for its radiopacity and compatibility,[4,16,17] and titanium (**Ti**) is favored in dental and orthopedic implants due to its strength and osseointegration capabilities.[18,19] Tungsten (**W**) is utilized in radiation protection due to its density and radiopaque properties,[20,21] and zirconium (**Zr**) is used in heart valves and dental implants.[22,23] Yet, the use and selection of metals in biomedical engineering require careful

[a]*Atatürk University, Faculty of Engineering, Department of Metallurgical and Materials Engineering, Erzurum 25240, Türkiye*
[b]*Biotechnology Centre, The Silesian University of Technology, B. Krzywoustego 8, 44-100 Gliwice, Poland. E-mail: malgorzata.wlodarczyk-buegun@polsl.pl*
[c]*Polymer Science, Zernike Institute for Advanced Materials, University of Groningen, Nijenborgh 4, 9747 AG Groningen, The Netherlands. E-mail: m.k.wlodarczyk@rug.nl*
† Electronic supplementary information (ESI) available. See DOI: https://doi.org/10.1039/d4bm01335b

evaluation, depending on their respective properties and targeted applications. For applications that include contact with the patient's body, examining the interactions of cells with metal surfaces is of great importance. Furthermore, it is crucial to conduct antimicrobial testing to evaluate the resistance of implants to bacterial infections by common pathogens, such as *Staphylococcus aureus* and *Escherichia coli.*[24,25] Current testing approaches primarily rely on using 2D cell cultures.[26–30] However, 3D cell culture models can offer significant advantages over conventional 2D models for evaluating the influence of metal coatings on surrounding tissues. Unlike 2D cultures, where cells are restricted to a flat surface, 3D scaffolds provide a biomimetic microenvironment, replicating the *in vivo* ECM architecture and enabling cells to interact with their surroundings in three dimensions. This promotes natural cell behaviors, such as differentiation, polarity, and matrix remodeling, which are crucial for the accurate evaluation of metal bioactivity or toxicity.[31] Additionally, 3D systems allow for the assessment of the influence of the material (here metals) on the cells at different distances from the actual coating, mimicking the diffusion dynamics in tissues *in vivo*. For example, a recent study has shown that a 3D human skin model with co-culture of keratinocytes and fibroblasts allows for a more accurate assessment of silicone implant's biocompatibility (revealing an inflammatory cytokine response) than a 2D model.[32]

Therefore, in this study, we propose a new 3D testing platform for in-depth characterization of biocompatibility of metals and metal coatings by integrating physical vapor deposition (PVD) coating technology with the 3D bioprinting method. To this end, we coated glass slides with **Ag**, **Nb**, **Ta**, **Ti**, **W**, and **Zr** metals using PVD to obtain metallic testing surfaces. These metals were used due to their broad applicability in the biomedical and tissue engineering fields. PVD was applied, as this is a versatile technology that allows for the deposition of various metals and metal alloys, providing a wide range of coating options for (implant) surfaces. The PVD process utilizes a vacuum chamber that is filled with a metal vapor source and a reactive gas such as nitrogen and oxygen. The metal vapor is generated by the formation of plasma on the surface of the metal target, which then condenses onto the substrate surface, forming a thin, homogeneous coating. The reactive gas is used to control the composition and properties of the deposited film.[33] PVD allows for high bonding strength, controlled coating thickness, high purity, and chemical stability. It can be applied at low temperatures, which is beneficial for coating heat-sensitive materials.[15,34]

A 3D tissue model was installed on PVD-produced coatings. The model was composed of a melt electrowritten (MEW) mesh integrated within methacrylated gelatin (GelMa). MEW is a 3D printing technique that uses molten polymers to create well-defined tissue scaffolds composed of precisely deposited thin fibers (typically with a diameter in a few micrometer range).[35,36] The fibrous structures can closely mimic the natural extracellular matrix architecture with tailored pore sizes and fiber orientation, critical for supporting specific cell adhesion, proliferation, and differentiation.[35–38] A mesh design of MEW scaffolds was chosen as this is the most studied and standardized architecture[39] that does not lead to specific cell alignment or migration patterns.[40] Integration with a GelMa hydrogel, known for its biocompatibility and biodegradability, provides a flexible matrix that mimics the characteristics of natural tissue and supports the 3D growth of cells.[41,42] Overall, while GelMa introduces a highly hydrated environment with cell adhesive motifs, the MEW support provides mechanical stability, prevents gel shrinkage due to the cells pulling on the material, and eases handling.

In this work, we show that the developed comprehensive testing platform allows for a detailed analysis of how different metals influence cell behaviour and bacterial growth at specific distances from the metal coating. We provide an easy-to-prepare tool for fast 3D screening of metallic materials and, from a broader perspective, the toxicity and biocompatibility of other compounds. Due to the application of the biofabrication approach, the composition, mechanical properties and structure of the model can be easily adapted to mimic different tissues, making the proposed platform adaptable and versatile.

2. Materials and methods

2.1 Coating of glass slides with metal ions

High purity **Ag**, **Nb**, **Ta**, **Ti**, **W** and **Zr** elements were coated on the surface of glass microscope slides (12 mm × 12 mm) using the PVD technique, as follows. Slides were first cleaned with 95% isopropyl alcohol (Sigma Aldrich) to ensure coating–surface adhesion and prevent impurity. For all the coatings, the process was carried out using magnetrons with a 3-inch diameter, 0.25-inch thickness, and 99.95% purity in the PVD system. The distance between the target and the substrate was set to 50 mm. After the slides were placed in the substrate holder, the cover of the PVD system was closed and the chamber was vacuumed. While waiting for the chamber to reach the vacuum level of 5×10^{-6} Torr, it was ensured that the chamber was free of impurities that may be present in the environment and may change the structure of the coating. Argon gas flow rate was adjusted to 100 sccm ($cm^3\ min^{-1}$) in order to create plasma in the device and splash the target atoms on the substrate material. The coating process was carried out for 20 minutes at 200 °C with a 100-watt Radio Frequency power supply.

2.2. Wettability testing of coated slides

The optical tensiometer (Dataphysics, Esr-N) was used to measure the wettability of various metal coatings. A 5 µl droplet of distilled water at a temperature of 25 °C was dripped, and after 10 seconds the image was captured and the angle was measured.

2.3. MEW scaffold printing

Fibrous scaffolds were fabricated using the MEW tool (Bio Scaffolder 3.3, GeSiM, Germany) with an operating tempera-

ture of 86 °C, 5.8 kV voltage, 13.6 Pa pressure, 3.6 mm nozzle to substrate distance, 1200 mm min^{-1} printing speed, and 0.3 mm metal nozzle diameter. Medical-grade polycaprolactone (PCL, PURASORB PC 12) was used. Printing was performed under the hood with 30% humidity at room temperature. Scaffolds with 350 um grid size and 30 layers were produced (see Fig. S1†). The FullControl GCode application was employed to generate the GCodes for printing.[43,44] After printing, the scaffolds were subjected to air plasma treatment using a Yocto plasma oven (Diener Electronics) to enhance the hydrophilic properties of the PCL scaffolds.[45] Plasma treatment was conducted for 5 minutes in a low-pressure environment using the device's built-in vacuum pump.

2.4. Mechanical and rheological characterization

To evaluate the stress–strain behavior of PCL scaffolds, tensile tests were performed using a hybrid rheometer (TA20 Instruments Discovery). Scaffolds were cut into 10 × 8 mm pieces, placed between the device clamps with a loading gap of 10 mm, and then tensile tests were performed at a constant pulling rate of 6 mm min^{-1} until the machine's limit was reached. The initial starting force was set to 0 N for every sample before stretching was initiated. The Young's modulus was determined based on the slope of the linear region of the stress–strain curve.

Rheological properties of 5%, 7.5% and 10% crosslinked GelMa were measured using a TA Instruments HR 20 rheometer. The storage modulus (G') and loss modulus (G'') were recorded and reported across a range of angular frequencies (ω = 0.1 to 100 rad s^{-1}) to evaluate the viscoelastic behavior of the material. A time sweep was conducted with a duration of 300 seconds at an axial strain of 0.1% and a frequency of 1.0 Hz.

Compression tests were conducted on 7.5% crosslinked GelMa samples using a TA Instruments HR 20 compression testing system. UV-crosslinked samples with 8 mm diameter and 0.15 mm thickness were placed in the rheometer. Stress–strain curves were recorded for the initial axial force in the following range: 0.1 N minimum and 0.2 N maximum. The hydrogels underwent a single compression cycle with a maximum strain of 30%, using a compression speed of 0.05 mm s^{-1}. Stress–strain curves were recorded during the process.

2.5. GelMa hydrogel integration with MEW meshes

The GelMa hydrogel (Polbionica Corporation, Poland), with a degree of substitution of 80% and a molecular weight greater than 15 kDa, was prepared in a phosphate buffer solution (PBS) with a pH range of 7.1–7.3.

2.5.1. Integration with MEW meshes for degradation studies. The composite scaffolds were prepared as follows: 7.5% non-sterile GelMa and 0.25% lithium phenyl-2,4,6-trimethylbenzoylphosphinate (LAP) were dissolved in PBS. Next, 25 μL of GelMa was placed on each metal coating, and the MEW scaffold was delicately placed in the middle using tweezers. Next, the hydrogel was crosslinked with UV light at a wavelength of 365 nm and an intensity of 1.2 mW cm^{-2} for 1 minute. The samples were then incubated at 37 °C in 1 mL Dulbecco's modified Eagle's medium (DMEM), changed every second day. The GelMa hydrogels with the MEW mesh were dried with a tissue to remove unbound liquid and then weighed along with the coated glass slides The samples were weighed on days 0, 1, 3, 7, and 14. The experiment was done in 6 replicates. The change compared to the initial weight was calculated as a percentage.

2.5.2. Preparation of the 3D model with fibroblast cells. NIH3T3 cells, passage number 29, were grown to confluency in 75 mL flasks containing 10 mL of medium (DMEM + 10% fetal bovine serum (FBS) + 1% penicillin/streptomycin). After removing the medium, dead cells were washed with PBS, and 3 mL of 1× trypsin (Sigma Aldrich) was added to the flasks and incubated for 5 minutes at 37 °C. Then, 6 mL of fresh DMEM was added, and the cell mixture was removed to the vial, centrifuged at 700 Relative Centrifugal Force (RCF) for 10 minutes and resuspended in the fresh medium. After cell counting, the cells were resuspended in GelMa solution at a density of 2 million per mL for further use.

The glass slides were cut into 10 × 10 mm, and the MEW meshes were cut into 8 × 8 mm to fit into a 12-well plate. GelMa in powder form and the coated slides were sterilized under UV light for 20 min. A hydrogel was prepared for each coating using 7.5% GelMa, 0.25% LAP, and 2 million cells per mL. 25 μL of cell-loaded GelMa was added on top of each coating type with a pipette, and, finally, a MEW scaffold was placed at a GelMa surface with tweezers. After the sinking of the MEW mesh, the hydrogel was crosslinked with UV light at a wavelength of 365 nm and a power of 1.2 mW cm^{-2} for 1 minute. The samples were then incubated under a 5% CO_2 atmosphere with 90% humidity. Samples were prepared in triplicate. The experimental protocol for this phase is depicted in Fig. S2.†

2.5.3. Cell culture in the composite material. Cell culture was performed for 14 days. A total of 1.5 mL of DMEM was added to each well and was replaced with fresh DMEM every other day.

2.5.4. Cell viability. To study cell viability, the Live/Dead assay was used. In short, cells were stained with fluorescein diacetate (FDA) (5 μg ml^{-1}) and propidium iodide (PI) solution (5 μg ml^{-1}) for 15 min at 37 °C in the dark. Imaging was performed with a confocal microscope (Olympus IX 81, Japan) using specific excitation/emission wavelengths for FDA (488/530 nm) and PI (561/620 nm) at 10× magnification. Three images per sample were analyzed using ImageJ software.

2.5.5. Cell metabolic activity. The cell metabolic activity of the samples was evaluated using an AlamarBlue assay, according to the protocol provided by the manufacturer, with fluorescence measurements (Synergy H4 Hybrid Reader, BioTec, USA) after 4 hours of incubation.[46] 200 μl of the medium containing the reagent was taken from each sample, transferred to a 96-well plate, and fluorescence was measured at excitation and emission wavelengths of 530 and 590 nm, respectively.

The reduction % was calculated according to the following equation:

$$\text{Alamar blue reduction}\% = \frac{\text{FI 590 of test agent} - \text{FI 590 of untreated control}}{\text{FI 590 of 100\% reduced alamarBlue} - \text{FI 590 untreated control}} \times 100$$

where Fl 590 is the fluorescence emission intensity of the following: test agent – the sample, untreated control – medium with AlamarBlue, reduced Alamar blue – from the autoclaved cell medium containing AlamarBlue.

2.5.6. Cell morphology. To visualize nuclei and actin, cells were fixed in 4% paraformaldehyde (Sigma-Aldrich) for 30 minutes and washed three times (3×) with PBS before treating with 0.1% Triton X for 20 minutes. After washing again with PBS (3×), the cells were incubated in 1% Gelatin (20 minutes) to block the activity of Triton-X, followed by another round of washing with PBS (3×). Then, the cells were incubated for 90 minutes in Phalloidin iFLuor 488 (1 : 1000 in PBS, (Abcam, UK)), washed with PBS (3×), and finally stained with 4′,6-diamidino-2-phenylindole (DAPI) for 30 minutes. A laser scanning microscope was equipped with two argon-ion lasers, providing wavelengths of 358 and 364 nm for DAPI, and 488 nm for iFluor (Olympus IX 81, Japan) was used. Images were obtained at 10× and 30× magnification.[47,48]

2.6. Scanning electron microscopy (SEM) imaging of the cells and coatings

All images were obtained using an FEI Quanta 400 FEG scanning electron microscope.

Coatings were visualized before and after cell culture, with the top and side view at 10 kV and 20 kV accelerating voltage under high vacuum conditions. The size of a coating in the cross-section view was measured and compared before and after the cell culture experiment.

The samples containing cells (from day 1, day 7 and day 14 of culture) were fixed in a 1 M sodium cacodylate solution (Sigma-Aldrich) containing 2.5% paraformaldehyde. This solution was also used to store samples prior to SEM imaging. For cryo-SEM, the samples were carefully washed with demineralized water, immersed in liquid nitrogen and imaged at 3 kV accelerating voltage, according to a previously developed protocol.[33] In addition, samples from day 14 were investigated under fully wet conditions at 3 °C and 750 Pa water vapor pressure using the ESEM mode and *in situ* dried at 3 °C and 100 Pa water vapor pressure. The dried samples were sputter-coated with Au (30 mA, 60 s) at room temperature and imaged under high vacuum conditions at 3 kV accelerating voltage.

2.7. Antibacterial testing

The antibacterial effect of metal coatings was investigated in a 3D model with two bacterial strains, Gram-negative *Escherichia coli* ATCC 25922 and Gram-positive *Staphylococcus aureus* ATCC 25923. Briefly, bacteria were cultivated in tryptic soy broth (TSB, Biomaxima, Poland) with the following composition: pancreatic digest of casein 17 g L^{-1}, soy peptone 3 g L^{-1}, sodium chloride 5 g L^{-1}, dipotassium hydrogen phosphate 2.5 g L^{-1}, and glucose monohydrate 2.5 g L^{-1}, pH 7.3 and harvested by centrifugation (5000 rpm, 10 min, 25 °C) in the mid-logarithmic phase. 0.5% agarose disks with 20% (v/v) of bacterial inoculum and 30% (v/v) of TSB medium diluted 1 : 10 were placed on the surface of metal coatings. After 18 h of incubation at 37 °C Live/Dead staining of bacteria with FDA (5 μg ml^{-1}) and PI (25 μg ml^{-1}) was performed. The control samples were prepared on a glass slide without the metal layer. All the samples, prepared in triplicate, were investigated under a confocal laser scanning microscope (CLSM) Olympus FluoView FV1000. The images were analyzed using ImageJ software.

2.8. Statistical analysis

Statistical analysis using the two-way ANOVA test with the Tukey *post-hoc* test in GraphPad Prism 8.0 was performed to determine statistical significance. The data were reported as mean value ± standard deviation and were considered significantly different at $*p \leq 0.05$, $**p \leq 0.01$, $***p \leq 0.001$, and $****$ $p \leq 0.0001$ ($N = 3$).

3. Results and discussion

3.1. Characterization of the coating

In this research, the PVD coating of glass slides was employed to mimic metallic implants and the cellular response to them was analysed. Materials recognized for their biocompatibility were used, *i.e.*, **Ag**, **Nb**, **Ta**, **Ti**, **W**, and **Zr**. Fig. 1 shows the following steps of the study.

The use of the PVD approach allows to obtain high purity metallic surfaces. Fig. 2 shows coating on microscope slides prepared using **Ag**, **Nb**, **Ta**, **Ti**, **W**, and **Zr**. The visible color differences can be assigned to the different physicochemical properties of the materials. The metallic grey appearance observed in metals like **Nb**, **Ta**, **Ti**, **W**, and **Zr** is due to their ability to reflect light across a wide, yet not entire, range of the visible spectrum. In contrast, silver (**Ag**) reflects almost the entire spectrum of visible light with exceptionally high efficiency, giving it a bright and distinctly white appearance.[49] The images also suggest high coating efficacy, which we confirmed by SEM as described in the following.

Fig. 3a shows SEM images of the surfaces of the coatings with different characteristics specific to each metal. The smallest grains were visible for **Nb**, **Ta**, and **W**, and the largest grain structure for **Ag**. Additionally, the coating thickness for all metals was between 100 and 200 nm, whereas for **Ag** a coating thickness of 730 nm was obtained. The sputtering rate of **Ag** was approximately 4.75 times higher than other metals due to its lower atomic binding energy, which makes it easier to eject atoms during the sputtering process. This resulted in the accumulation of more metal ions, causing the grains to become larger as the coating thickness increased.[50] In the PVD method, coatings generally grow in a columnar pattern and, subsequently surface roughness at the microscopic scale

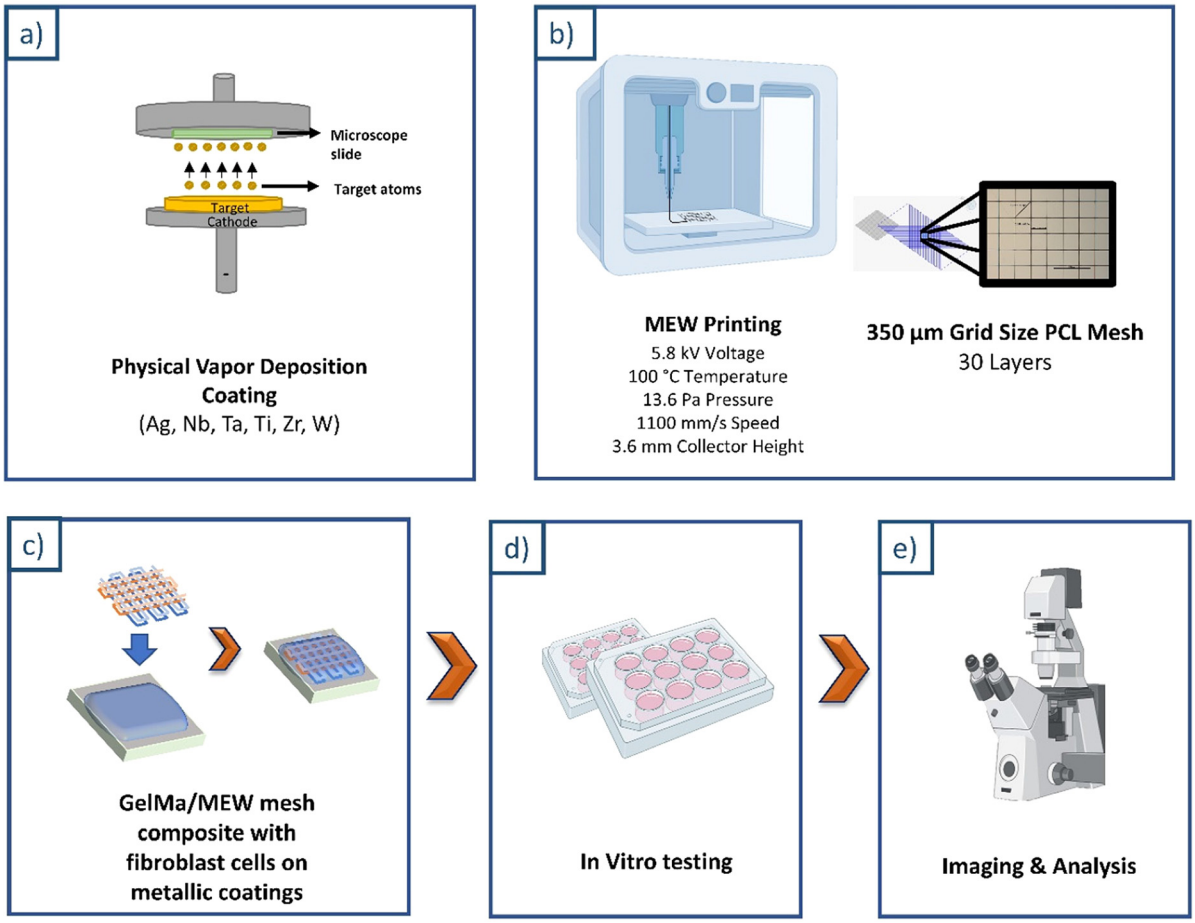

Fig. 1 Steps of the study. (a) PVD metallic coatings of the slides; (b) PCL mesh printing using MEW; (c) placement of the GelMa/MEW mesh composite scaffold containing fibroblasts on coated slides; (d) *in vitro* testing; and (e) imaging and analysis of samples.

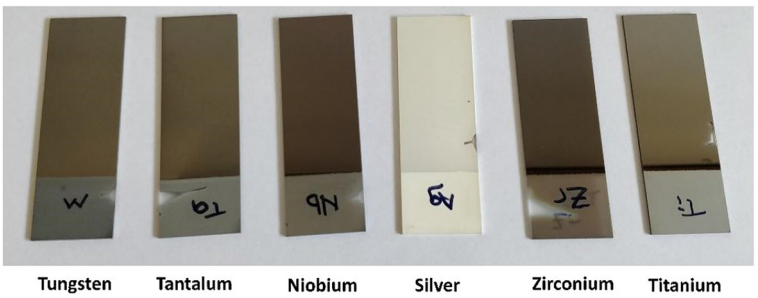

Fig. 2 PVD coatings with different metals.

occurs. The low deposition rates and high substrate temperatures result in the formation of thin and smooth films. High deposition rates and low substrate temperatures lead to the observation of columnar structures. Intermediate deposition rates and temperatures can result in a granular structure. This provides a way to obtain controlled, application-specific coating structures.

Water contact angle measurements were performed to estimate the wettability of the surfaces. A contact angle greater than 90° indicates that the surface is hydrophobic (water-repellent) while a contact angle below 90° indicates that the surface is hydrophilic (water-attracting).[51] The ranking of the coatings from most hydrophobic to most hydrophilic states is **Ag**, **Zr**, **Ta**, **Nb**, **Ti**, and **W** (Fig. 4). **Ag** exhibited the most hydrophobic character, whereas **W** showed highly hydrophilic properties. The results are directly related to the trend in the changes of the surface morphology (Fig. 3). It can be observed that the rougher surfaces tend to be more hydrophobic, while

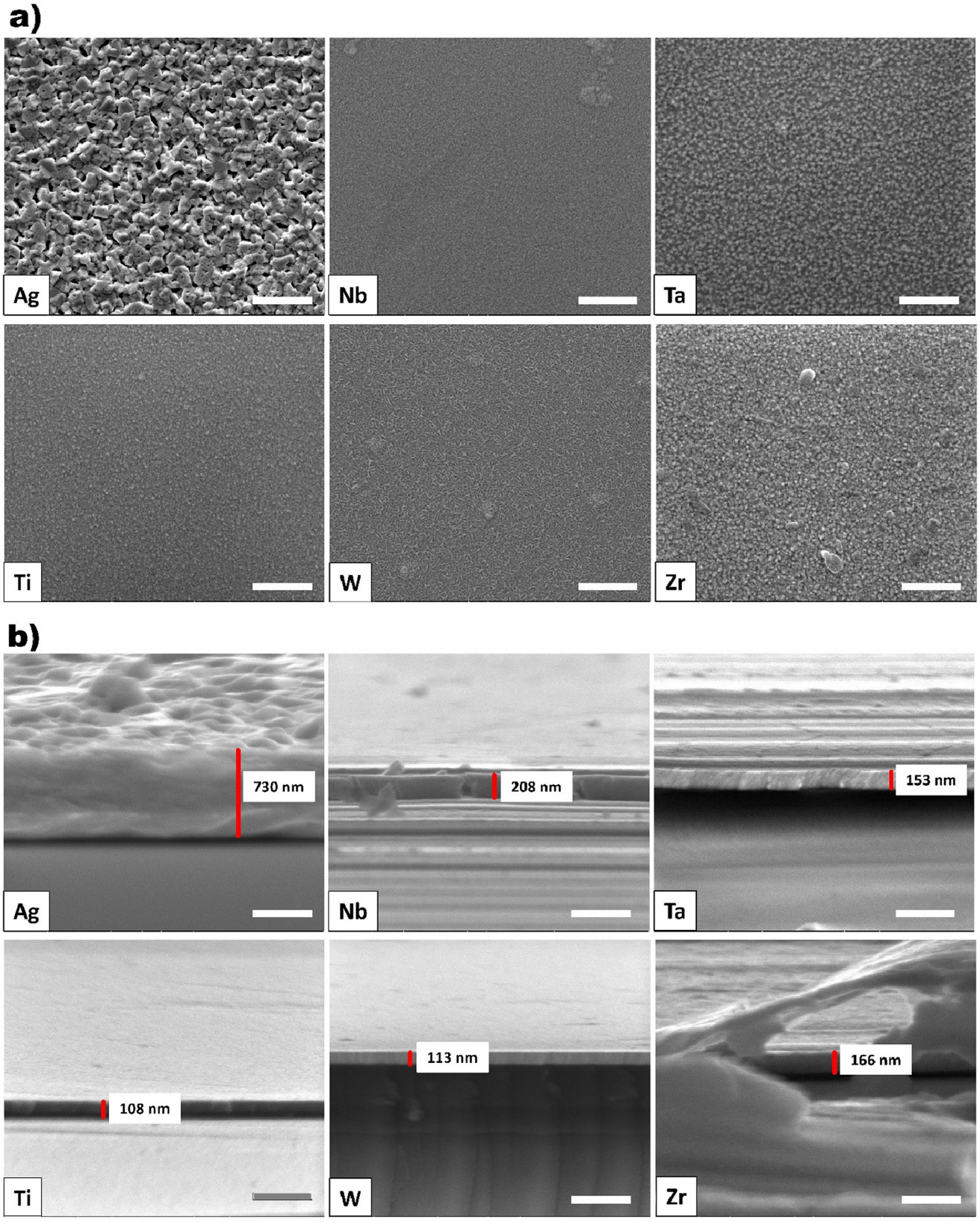

Fig. 3 SEM images of PVD metallic coatings on glass before cell culture studies (different metals are indicated in the left bottom corners). (a) Top view; (b) cross-sectional view with a measured coating thickness (scale bar 500 nm).

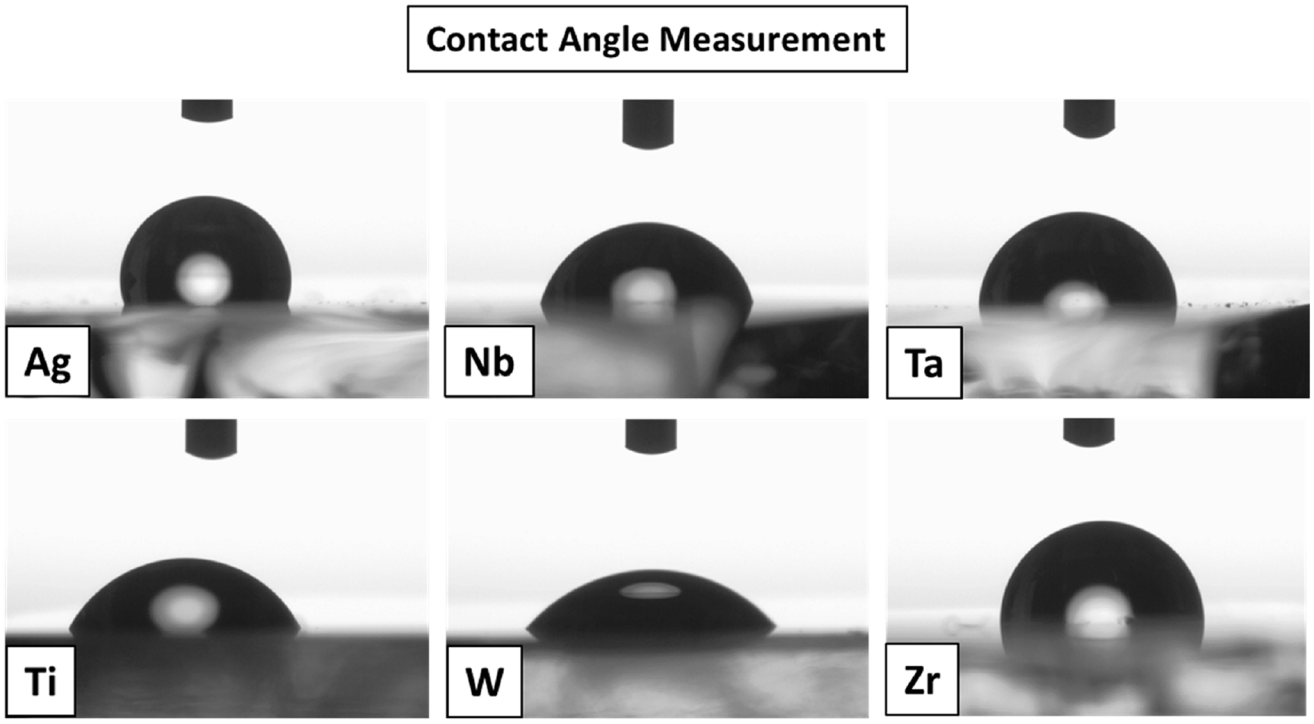

Type of metal	Ag	Nb	Ta	Ti	W	Zr
Water contact angle (°)	107.2± 3.25	79.7± 3.77	87.6± 3.87	64.37± 1.19	56± 2.05	87.87± 2.97

Fig. 4 Contact angle measurement of PVD-coated samples.

smoother surfaces are more hydrophilic. In general, metals tend to be hydrophilic due to their high surface energy and tendency to form oxide layers when exposed to air.[52] However, surface roughness can influence the intrinsic wettability of a material. Rough surfaces can either enhance hydrophobicity by trapping air pockets, which prevents water from fully wetting the surface, or increase hydrophilicity through capillary effects that promote water spreading.[52,53] For the final properties, both, chemical composition and surface structure play a decisive role.

The hydrophobicity of a coating was tested as it could influence the interaction with the biofabricated model and also affect cell–material interactions. It is expected that hydrophilic surfaces will interact better with the hydrogel-based model. On the other hand, while a certain degree of hydrophobicity can be beneficial for promoting cell adhesion and proliferation, surfaces that are too hydrophobic can hinder these processes.[54,55]

As the biofabricated 3D scaffolds (*i.e.*, GelMa component) were prepared in PBS, the stability of the coatings was tested in PBS prior to cell studies. It was found that the PBS droplet completely dissolved the **W** coating surface after 24 hours (Fig. S3†). All other metal coatings were stable for 14 days. **W** is known for its excellent mechanical and thermal properties, high melting point, and corrosion resistance in many environments. However, at the same time, **W** is susceptible to corrosion in certain environments, including PBS solutions. At higher pH values, this oxide layer would be expected to dissolve, leading to accelerated corrosion. Yet, the corrosion behavior of **W** in PBS was most probably mainly influenced by the PBS concentration and the presence of other ions like chlorides.[56] The complex phosphate species from PBS can be formed and attack the oxide layer, leading to corrosion.[57]

3.2. Characterization of the components of the biofabricated scaffold

The biofabricated model was composed of the GelMa hydrogel with the integrated MEW mesh. The components were characterized with regard to mechanical properties.

3.2.1. Rheological testing of the GelMa component. To determine the GelMa concentration appropriate for the 3D model, rheology tests were conducted for hydrogels composed of 5%, 7.5%, and 10% GelMa after UV crosslinking (Fig. 5a). To determine the relative elastic (G' storage modulus) and viscous (G'' loss modulus) components, we conducted frequency sweep measurements ranging from ω = 0.1 to 1000 rad s^{-1} at γ = 1%. G' was higher than G'' for all 3 samples, indicating dominant elastic behavior. The storage modulus (G')

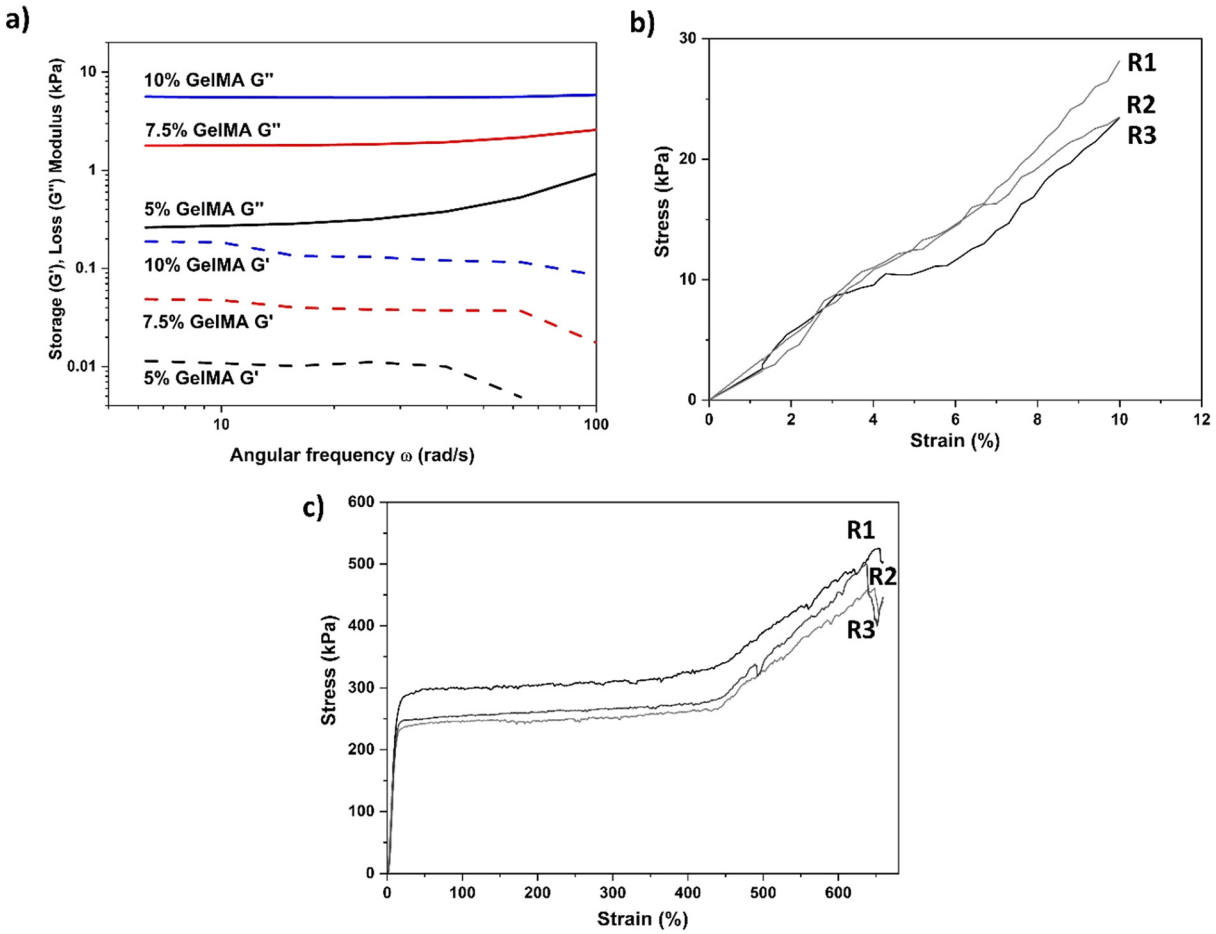

Fig. 5 (a) Frequency sweep and stress–strain graph obtained in rheology testing of GelMa after 1 min UV curing. (b) Compression test of 7.5% crosslinked GelMa (samples in triplicate: run 1, 2, and 3). (c) The tensile testing of MEW scaffolds (samples in triplicate: run 1, 2, and 3,).

values were as follows: 5.58 kPa for 10% GelMa, 3.98 kPa for 7.5% GelMa, and 1.06 kPa for 5% GelMa. GelMa at a concentration of 10% exhibited a relatively high storage modulus (G') posing the risk of hampered cell proliferation and migration.[58] Conversely, GelMa at a 5% concentration was found to possibly lack the necessary self-supporting properties. Therefore, we selected the 7.5% concentration as it maintained a balance between stiffness and flexibility, providing an ideal environment for cell proliferation.

Compression testing was performed for the crosslinked GelMa hydrogel at 7.5% concentration, and the obtained stress and strain curve is presented in Fig. 5b. The compression modulus value was determined to be *ca.* 190–230 kPa.

3.2.2. Tensile testing of MEW scaffolds. The elasticity modulus of the MEW meshes in the tensile mode was determined to be 19 kPa (Fig. 5c). The scaffold mesh exhibited plastic deformation after an elastic strain range of 15–20%. Breakage of the scaffolds occurred above the applied strain of 430% (Fig. 5c). These results align with the high ductility demonstrated in the tensile test results reported before.[38] Though, the tensile modulus of scaffolds produced by melt electrowriting (MEW) varies depending on the material type, number of layers, layer thickness, geometry, manufacturing parameters, and microstructure. Therefore, the parameters in the literature may differ.[59–61] Yet, in general, the MEW meshes are characterized by a relatively low stiffness and pronounced ductility. This may prove beneficial for applications necessitating substantial flexibility and a high capacity for deformation prior to failure.

3.3. Biofabricated scaffolds

The primary goal of the study was to develop an advanced 3D platform for testing metallic bioimplants and coatings. To this aim, we intended to create a 3D tissue model, utilizing both the MEW mesh and the GelMa hydrogel, to simulate the features of natural tissues. This model was further used for a detailed study of coatings and their interactions with biological systems.

The GelMa hydrogel was selected for its remarkable capacity to emulate the natural tissue milieu, fostering cell proliferation. Its hydrophilic nature and adjustable mechanical properties render it ideal for fabricating scaffolds that not only support cellular growth but also facilitate tissue regeneration.[62] In contrast, the MEW mesh, produced through a

precise electrowriting process, was implemented to provide a durable and supportive framework. The framework, composed of micro-sized fibers, can support the formation of complex networks, further optimizing the environment for cell attachment and proliferation.[37] The scaffolds were fabricated from PCL which is a gold standard material in the MEW approach, well known for its biocompatibility, low toxicity, high flexibility and slow degradation rate.[63]

It was observed under a microscope that 20 μm was a sufficient volume to fully cover the MEW scaffold, whereas 30 μm was excessive, as shown in Fig. S4.† Taking into account the possibility of some liquid evaporation and hydrogel shrinkage during UV curing, the amount of hydrogel to be integrated with the mesh was set to 25 μm. The hydrogel was effectively mixed with the cells, leading to homogeneous cell distribution (see Fig. 6), and successfully integrated with the MEW mesh (see Fig. S4†). The final scaffolds were on average 450 μm high and were virtually divided into 3 zones (see Fig. 9) for further characterization of their biological performance. Each zone was 150 μm high; zone 1 was the closest to the glass surface, while zone 3 was the outermost one.

3.3.1 Characterization of cell viability, morphology and behavior in the biofabricated 3D model. The cell-laden hydrogel integrated with MEW meshes was used to investigate cell viability and proliferation when cultured in contact with metal-coated substrates. NIH3T3 fibroblast cells were employed in cell culture studies due to their well-characterized behavior and widespread use across scientific research.[64] The cell concentration was adjusted to 2 million cells per 1 mL in a GelMa solution.

The Live/Dead assay was used to assess the distribution and viability of cells within 3D cultures over intervals of 1, 7, and 14 days. Live/Dead cell imaging analysis (no distinction to zones) revealed that at day 1 (Fig. 6a and 7a) samples coated with **Ag**, **Nb**, **Ta**, and **Ti** exhibited superior cell viability, at the levels of 89%, 97%, 86%, 97% and 91%, generally suggesting no toxic effect. The **W** coating's dissolution in the cell medium significantly reduced cell viability to 66%. The increase in the number of dead cells was further observed at day 7 (63% viability) due to the continued toxic influence of **W** ions. By day 7 (Fig. 6b and 7a), the adverse effects of **Ag** also became apparent, and the cell viability was at the level of 42%. Day 14 imaging (Fig. 6c and 7a) shows that **Ag**'s toxicity persisted as proved by the viability of 25.5%; **Nb**, **Ta**, **Ti**, and **Zr** maintained high viability, at the level of 85%, 89%, 86%, and 80%, respectively. For **W** samples, after the effects of the metal ions diminished, cell survival resumed, reaching a level of 96% at day 14, indicating a recovery from earlier adverse impacts. This pattern underscores the nuanced interactions between cell viability and metallic environments within 3D cultures, highlighting the variable effects of different metal ions on cell viability over time. Compared to 2D models, the 3D cell culture model allows for unique observations, such as cell migration within a structured matrix, cellular network formation, and tissue-like response.[65,66]

Furthermore, the Alamar Blue reduction assay was used to measure cell metabolic activity. An increase in reduction indi-

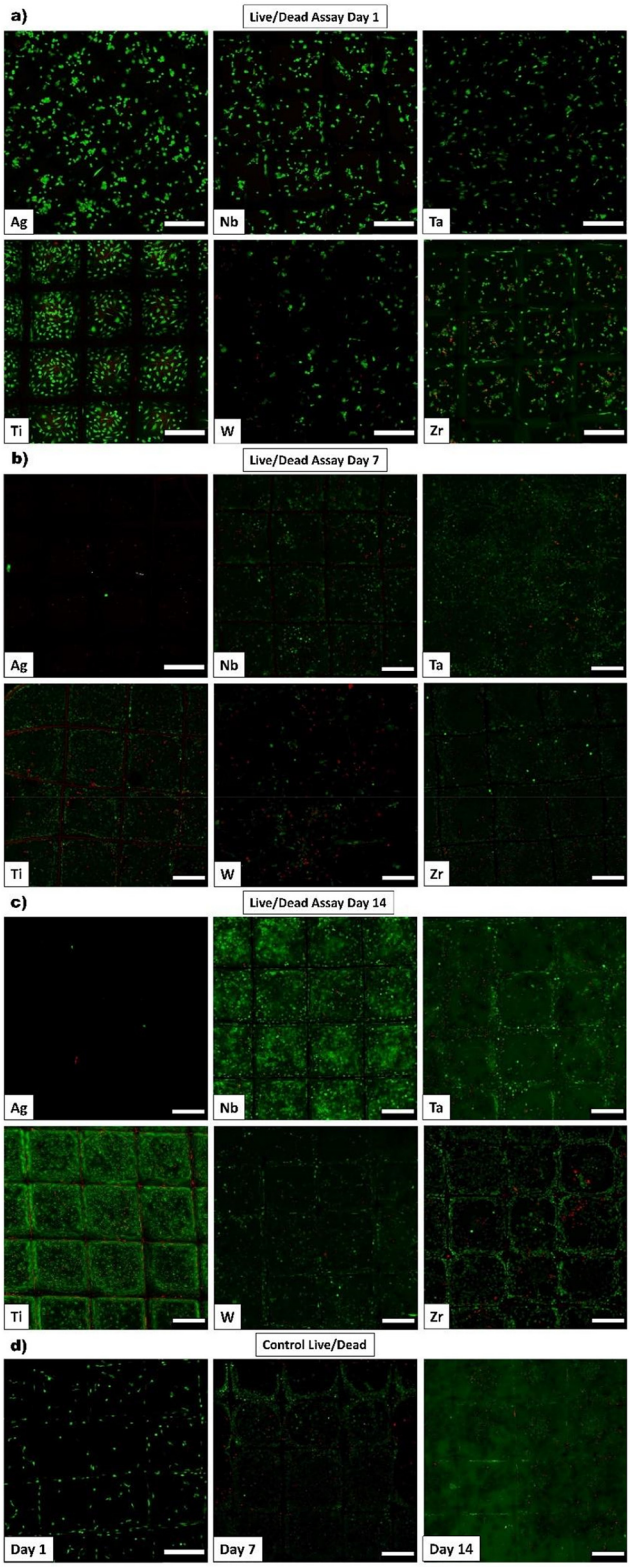

Fig. 6 Live/dead assay images of cells in the *in vitro* models placed at the coatings (green: live, red: dead): (a) day 1; (b) day 7; (c) day 14; and (d) control – cells on the glass slides (scale bar 200 μm).

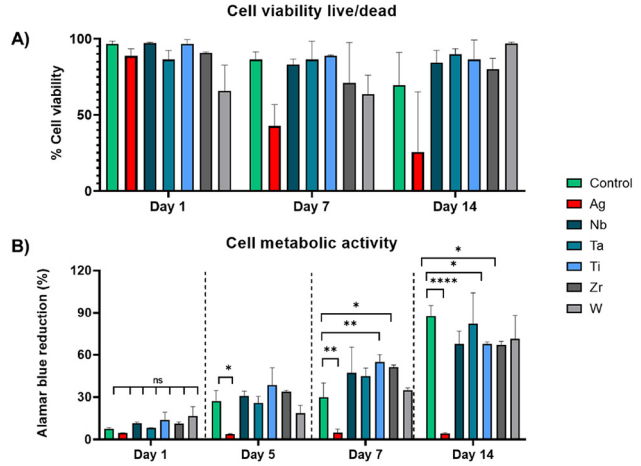

Fig. 7 (A) Bar graph showing cell viability percentage calculated from live and dead cell images (n = 3). (B) Alamar Blue assay representing the cell metabolic activity on the control and coated samples (n = 3). The data were reported as mean value ± standard deviation (*$p \leq 0.05$, ** $p \leq 0.01$, ***$p \leq 0.001$, and **** $p \leq 0.0001$). Only differences with control samples are marked.

cates higher metabolic activity. The metabolic activity of cells in the 3D environment on metallic coatings was measured on days 1, 5, 7 and 14 and compared with the controls (Fig. 7b). After 24 hours of culture, no significant differences were noticed for any metallic coating and controls. After 5 days of culture, the cellular activity for **Ag** was significantly low compared to the control and all other coatings. **W** similarly showed a low reduction rate with a mean value of 19%. On day 14, the highest reduction rate was determined in the control sample, with significantly lower cellular activity of **Ti** and **Zr**, which could be attributed to the relatively high population of the cells and difficulty in nutrient and oxygen transport. However, **Ta** and **Nb** showed no difference when compared to the control samples on day 14.

To further evaluate cell performance, cells in a biofabricated 3D model were stained to observe nuclei (DAPI) and actin filaments (Phalloidin) on day 1, day 7, and day 14 (Fig. 8a–c). Control samples are presented in Fig. 8d. After 24 hours of culture, it was observed that the cells were evenly distributed in the hydrogel between the MEW PCL fiber without forming any clumps. Furthermore, the samples coated with **Ti** and **Zr** displayed elongated cytoskeletal extensions. In contrast, the cell morphology of **Ag**, **Nb**, **Ta**, and **W** samples resembled that of control samples with a rounded shape. At one week of culture, the toxic effect of **Ag** became evident, as only a few rounded cells were observed indicating that the **Ag** ions had disrupted the normal cellular processes, ultimately leading to cell death. The negative impact of the metal ion release on cells in terms of viability and proliferation, as detected by Live/Dead and Alamar Blue assay, was confirmed by fewer cells visible in the scaffolds for **W**-coated samples. **Nb**, **Ta**, **Ti**, and **Zr** samples had a high number of nuclei when compared to **Ag** and **W**. Interestingly, we observed at the end

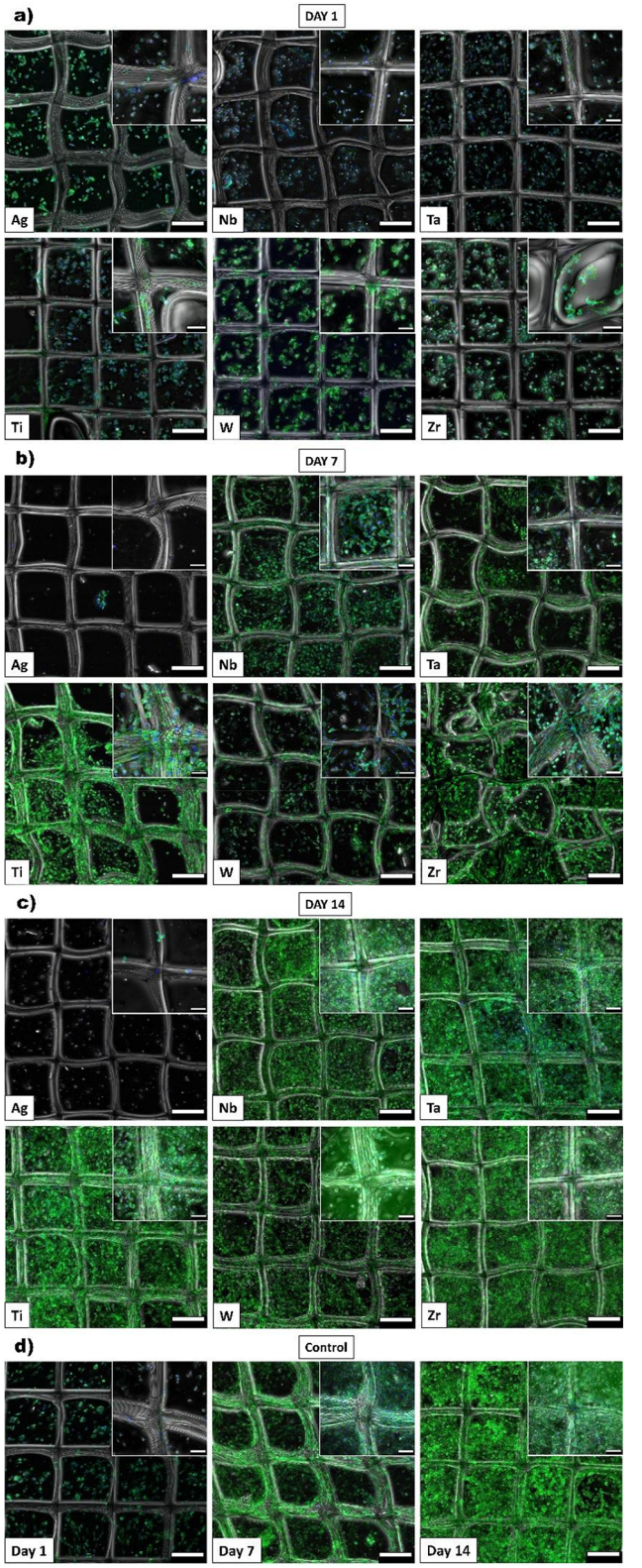

Fig. 8 Confocal images (blue: nuclei, green: actin): (a) day 1; (b) day 7; (c) day 14; and (d) control samples on the glass slides (scale bar 200 μm).

of the 14-day culture that fractures and deterioration occurred in the **Zr** metallic coatings, while **Ag** separated from the glass surface as a foil.

The growth mechanism of NIH-3T3 fibroblast cells in 3D cell culture can be different from their growth in traditional 2D cell culture.[67] In the 3D culture, NIH-3T3 cells can form spheroids or clusters, unlike their uniform adherence and spreading onto the flat surface of the culture dish. When cell-laden hydrogel is reinforced by the PCL scaffold mesh, the cells can attach and proliferate on the mesh surface. The hydrogel provides a 3D environment that allows for cellular organization and differentiation, while the PCL scaffold provides a structural framework that supports cellular growth. We observed that for all the samples, besides Ag, at later time points, the fibroblasts aligned and migrated along the fibers of the PCL scaffold mesh, the effect was observed in other studies before.[68]

To improve the clarity of investigating how coatings affected cell behavior and proliferation and to define zonal-specific activities in 3D scaffolds, biofabricated models were divided arbitrarily into zones, as illustrated in Fig. S5.† Three zones of *ca.* 150 μm were selected. Zone 1, which was close to the metallic substrate, zone 2 in the middle, and zone 3 on the top of the scaffold.

Based on the observations in Fig. 9, it appeared that in the control sample (hydrogel/mesh composite on uncoated glass slide), cells primarily grew on the hydrogel located between the PCL fibers. The cell density was lower in zone 1, near the glass surface, than in zone 2 and the lowest in zone 3 (Fig. 9d). We hypothesise that the cells sedimented slightly during the time of culture, leaving the upper part less populated. We also considered that zone 1 could be slightly negatively affected by the worst nutrient and oxygen supply or by the cell preference to attach to a GelMa/PCL material rather than to the glass slide.

In zone 1, a dense cell population was seen on the surface of **Nb**, **Ta**, **Ti**, and **W** coatings, indicating good cell adhesion and, therefore, high biocompatibility, while **Zr** had relatively fewer cells in this area. In contrast, almost no cells were observed on the surface of the **Ag** sample (Fig. 9a). As demonstrated in Fig. 9b, the cellular density in the **Nb** and **Ta** samples in zone 2 was comparable to that of zone 1. Notably, **Zr** exhibited increased cell proliferation in zone 2 compared to zone 1. **Ag** samples did not contain any cells, and the number of cells in **Ti** and **W** was relatively lower than that observed in zone 1. In zone 3 a lower number of cells were seen in all the samples with metal coatings (Fig. 9). This is due to the gravitational effect causing cells to move towards lower regions. This differential cell behavior across zones highlights the varying biocompatibility of the tested metallic coatings, with **Nb**, **Ta**, and **Ti**, demonstrating more favorable conditions for cell growth compared to **Zr** and **Ag**. **W**-containing samples revealed good cell performance, however, the coating was not stable, and so the conclusion about metal biocompatibility should not be directly drawn. In the future, studies with live-cell tracking could be performed to further observe cell migration and interaction directly with the coatings.

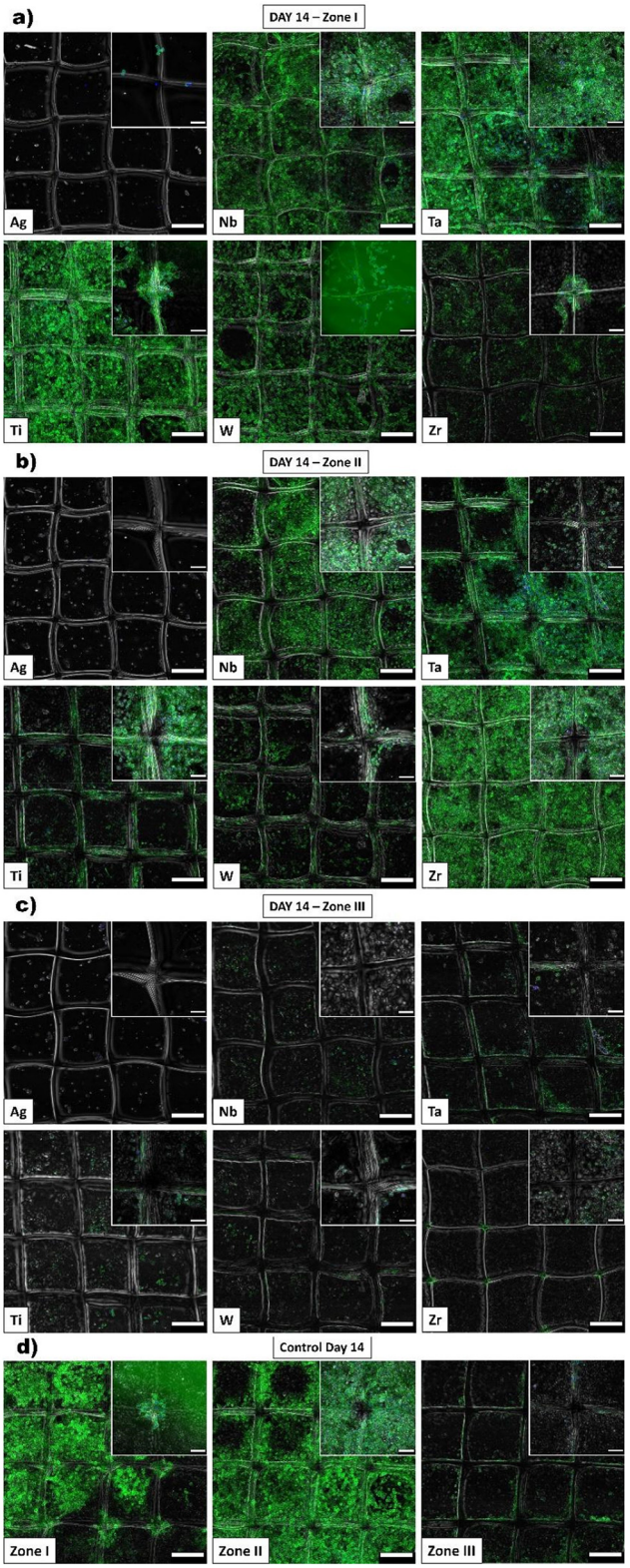

Fig. 9 Day 14 confocal images in different zones (blue: nuclei, green: actin): (a) zone 1; (b) zone 2; and (c) zone 3 of the coated samples (scale bar 200 μm, inner images 100 μm).

In order to analyze cell morphology and density in a liquid-free environment, cryo-SEM imaging was conducted on cells within a 3D model on metal-coated substrates (see Fig. S6†). The results revealed that PCL scaffold meshes maintained the structure of the hydrogel intact for up to 14 days during cell culture. However, cell morphology could not be clearly seen due to embedment inside the frozen hydrogels. Therefore, ESEM imaging was performed on dried hydrogels to investigate cell morphology and growth within the hydrogel. Based on this imaging (see Fig. 10), high cell density was observed in all other coatings with good cell–cell connections, except for **Ag**.

3.3.2. Degradation of GelMa scaffolds. SEM imaging allowed for the measurement of the thickness of the coatings before (day 0) and after (day 14) cell culture study (see Table 1). As previously mentioned, the **W** coating had completely degraded from day 1. The degradation % in the **Ta** coating was smaller than all other metals, indicating the most stable coating. The thickness of the **Ag**, **Nb**, and **Ti** coatings decreased by approximately 100 μm in 14 days, and that of the **Zr** coating by approximately 50 μm.

Table 1 Degradation of the coatings based on the height measurements of the cross-sectional profile of the coatings

Metal coatings	Day 0 (μm)	Day 14 (μm)	Degradation rate (%)
Ag	730	600	17.8
Nb	208	101	51.4
Ta	153	144	5.8
Ti	153	64	58.1
W	108	0	100
Zr	166	125	24.6

3.4. Anti-bacterial testing

The antibacterial effect of **Ag**, **Nb**, **Ta**, **Ti**, **W** and **Zr** coatings and control samples were investigated in a 3D model with two bacterial strains, Gram-negative *Escherichia coli* ATCC 25922 and Gram-positive *Staphylococcus aureus* ATCC 25923 (see Fig. 11). After 18 hours of incubation, a Live/Dead assay was performed. The presence of red cells indicates dead bacteria and good antibacterial properties of the coating, while cells in green are alive, suggesting poor antimicrobial properties. **Ag** coating showed a significant reduction in bacterial colonies (only dead cells in red were visible), indicating a strong antibacterial effect against both *E. coli* and *S. aureus*. **W** also exhibited antibacterial properties, though to a lesser extent than **Ag**, likely due to its dissolution in PBS in 24 hours which diminished its antibacterial effect. **Ta** demonstrated antibacterial activity primarily against *S. aureus*, possibly due to structural differences between the bacterial species. **Ti** and **Zr** coatings showed moderate antibacterial effects, with some reduction in bacterial colonies but not as pronounced as **Ag** or **W**. **Nb** coatings had the least antibacterial effect, with minimal reduction in bacterial colonies compared to the control.

To summarize, when evaluating cell viability alongside antibacterial properties, **Nb** and **Ti** displayed neither toxic nor

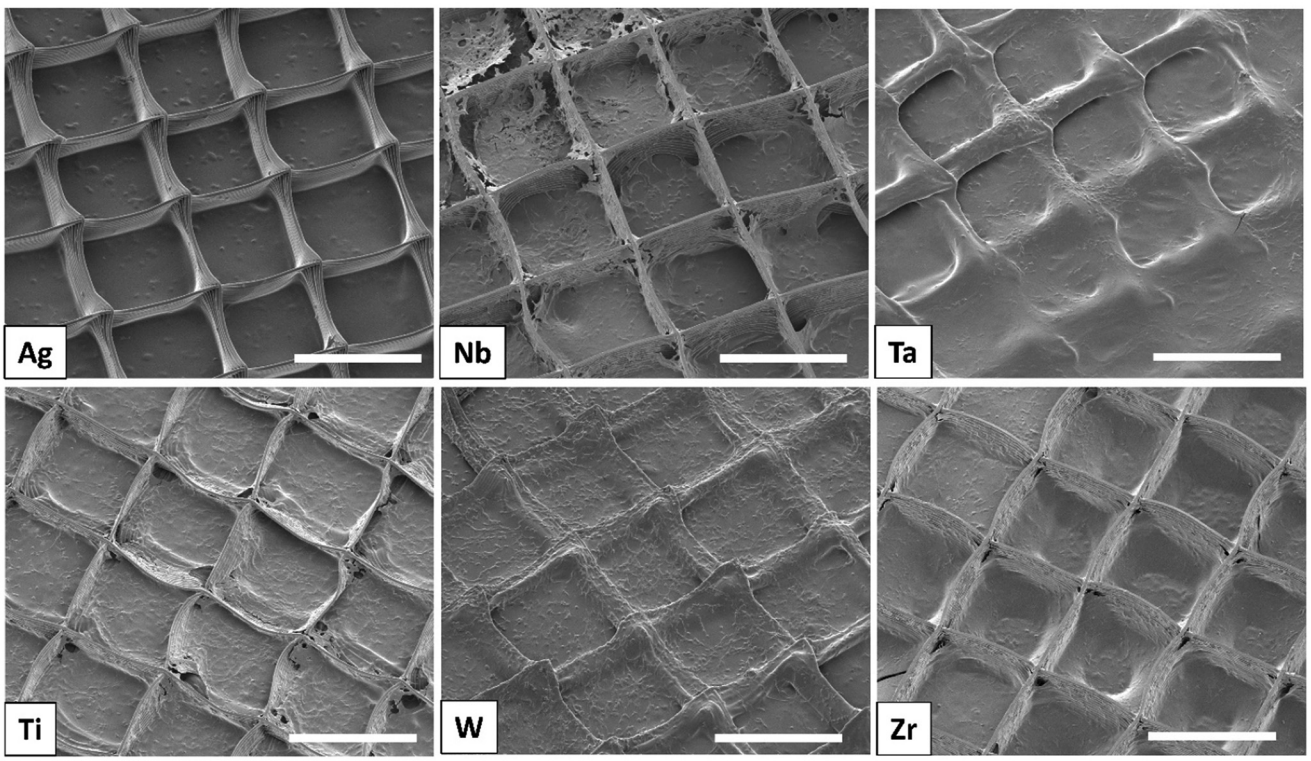

Fig. 10 Day 14 SEM images of the 3D biofabricated models (scale bar 400 μm).

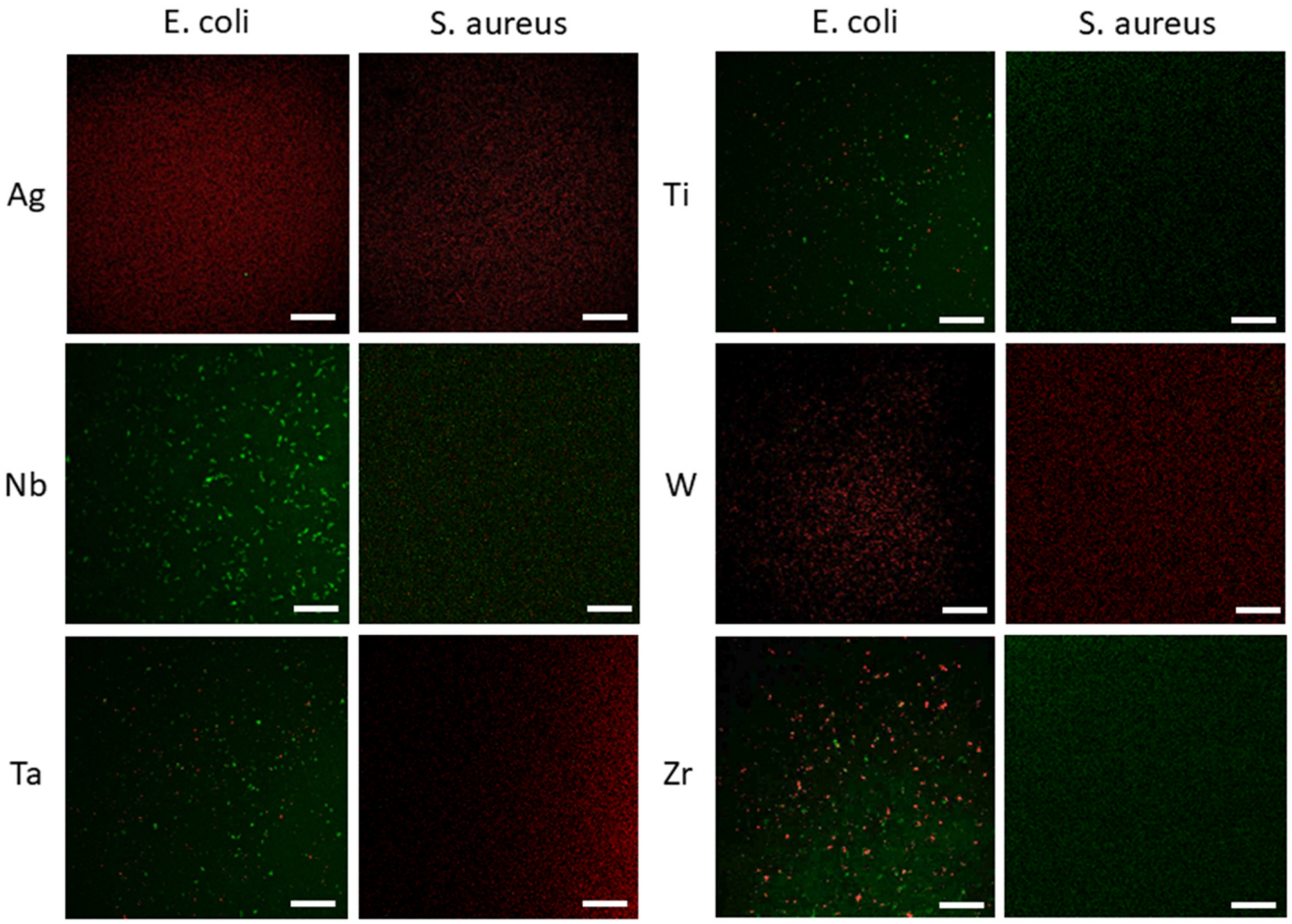

Fig. 11 Anti-bacterial testing of the **Ag**, **Nb**, **Ta**, **Ti**, **W** and **Zr** coatings and control samples after 18 h of incubation with *E. coli* and *S. aureus* embedded in the 3D agarose model (scale bar 200 μm).

strong antibacterial effects. **Ti** is known for inherent antibacterial properties, but in our study probably the concentration of the released ions was not enough to exert an antibacterial effect on cells additionally protected by agarose. **Ta** demonstrated no toxic effect on cell viability and exhibited antibacterial properties specifically against *S. aureus*. **Ta** exhibited antibacterial activity only against *S. aureus*, which can be ascribed to structural differences between these two bacteria. *E. coli* as a Gram-negative species is additionally protected by the outer membrane which can greatly influence the metal's uptake. As *Staphylococci* are responsible for implant infections in orthopedic implants, **Ta** coatings can be used with high cellular compatibility in areas where such infections are likely to occur.[69] In contrast, **Zr** showed more toxicity in terms of cell viability compared to **Ti**, **Nb**, and **Ta**, but it did exhibit antibacterial activity against *E. coli.* **Zr** can influence essential metabolic pathways and disrupt the cell membranes of the bacteria, which can lead to bactericidal or bacteriostatic effects.[70] Taking together these results, **Ta** coatings were identified as the most biocompatible and beneficial.

4. Conclusions

This study explored a biofabricated 3D model as a testing platform for analyzing the response of the cells exposed to the model biomaterial, *i.e.* the metal coating, in 3D. The model was composed of a MEW scaffold integrated into 7.5% GelMa hydrogel, and divided into three zones for analysis of cell performance at a different distance from the biomaterial. Such a prepared system was placed on high-purity metallic coatings (**Ag**, **Nb**, **Ta**, **Ti**, **W**, and **Zr**) obtained on glass slides with PVD technique.

The experimental methodology encompassed analysis of the physical properties of these coatings and assessing their impact on NIH3T3 fibroblast cell viability, and proliferation, during 14-day culture. Furthermore, the study evaluated the infection resistance of the scaffolds through antibacterial tests against *S. aureus* and *E. coli*. The study found that most coatings maintained their integrity, except for **W**, which dissolved in PBS within 1 day. Results indicated varying degrees of cellular activity and viability when in contact with the different metal coatings, with **Ag** exhibiting toxicity and **Nb**, **Ta**, **Ti**, and

Zr supporting cellular activity. The variations in cell behavior at different distances from the metal coatings were observed, proving the potential of the model for capturing more detailed biocompatibility profiles, closer to the anticipated *in vivo* performance. In the future, to obtain a more refined characterization of cellular responses to metal ions within the system, the incorporation of additional cellular marker analyses and proteomic profiling is envisioned. The antibacterial properties varied across metals, with **Ag** and **W** demonstrating strong antibacterial effects, particularly against *E. coli* and *S. aureus*. This nuanced understanding of metal biocompatibility within 3D tissue models underscores the potential of **Ta**, **Nb**, **Ti**, and **Zr** as biocompatible materials, with the most advantageous features of **Ta**, and suggests careful management of silver's antibacterial properties to mitigate cytotoxic effects.

By offering an idea of a novel 3D *in vitro* testing platform, allowing zone-specific analysis of cellular response, this study provides a valuable framework for future research on safe and effective materials for biomedical applications, for example, to enhance the efficacy and safety of metallic implants in medical settings.

Data availability

The data supporting this article have been incorporated as part of the ESI.† The data utilized and analyzed in the present study are obtainable from the corresponding author upon reasonable request.

Conflicts of interest

There are no conflicts to declare.

Acknowledgements

T. C. S would like to acknowledge financial support from the Scientific and Technological Research Council of Türkiye (TÜBİTAK) BIDEB-2219 Postdoctoral Research Program (Grant No. 1059B192100111). P. K. R. G., J. Z. P. and M. K. W.-B. acknowledge financial support from the Polish National Agency for Academic Exchange (NAWA, Polish Returns grant no. PPN/PPO/2019/1/00004/U/0001). M. K. W.-B. acknowledges the National Science Centre, Poland (NCN, OPUS grant no. 2020/37/B/ST5/00743). We thank Marcus Koch (INM – Leibniz Institut for New Materials, Germany) for support in electron microscopy and D. Parisi (University of Groningen) for the discussion on rheology.

References

1 X. Wang, D. Zhang, Y. Pratap Singh, M. Yeo, G. Deng, J. Lai, F. Chen, I. T. Ozbolat and Y. Yu, *Engineering*, 2024, **42**, 121–142, DOI: **10.1016/J.ENG.2024.04.023**.

2 D. Duraccio, F. Mussano and M. G. Faga, *J. Mater. Sci.*, 2015, **50**, 4779–4812, DOI: **10.1007/S10853-015-9056-3/FIGURES/12**.

3 S. Thanigaivel, A. K. Priya, D. Balakrishnan, K. Dutta, S. Rajendran and M. Soto-Moscoso, *Biochem. Eng. J.*, 2022, **187**, 108522, DOI: **10.1016/J.BEJ.2022.108522**.

4 S. Thanka Rajan, B. Subramanian and A. Arockiarajan, *Ceram. Int.*, 2022, **48**, 4377–4400, DOI: **10.1016/j.ceramint.2021.10.243**.

5 M. Al Sharabati, R. Sabouni and G. A. Husseini, *Nanomaterials*, 2022, **12**, 277, DOI: **10.3390/NANO12020277**.

6 V. Huynh, N. K. Ngo and T. D. Golden, *Int. J. Biomater.*, 2019, **2019**, 3806504, DOI: **10.1155/2019/3806504**.

7 V. V. Ramalingam, P. Ramasamy, M. Das Kovukkal and G. Myilsamy, *Met. Mater. Int.*, 2020, **26**, 409–430, DOI: **10.1007/S12540-019-00346-8**.

8 C. W. Kang and F. Z. Fang, *Adv. Manuf.*, 2018, **6**, 20–40, DOI: **10.1007/S40436-017-0207-4**.

9 T. C. Senocak, K. V. Ezirmik and S. Cengiz, *Mater. Today Commun.*, 2022, **32**, 103975, DOI: **10.1016/j.mtcomm.2022.103975**.

10 S. B. Yaqoob, R. Adnan, R. M. Rameez Khan and M. Rashid, *Front. Chem.*, 2020, **8**, 376, DOI: **10.3389/fchem.2020.00376**.

11 C. G. A. Das, V. G. Kumar, T. S. Dhas, V. Karthick, K. Govindaraju, J. M. Joselin and J. Baalamurugan, *Biocatal. Agric. Biotechnol.*, 2020, **27**, 101593, DOI: **10.1016/j.bcab.2020.101593**.

12 N. F. Mohammad, R. N. Ahmad, N. L. Mohd Rosli, M. S. Abdul Manan, M. Marzuki and A. Wahi, *Mater. Today Proc.*, 2021, **41**, 127–135, DOI: **10.1016/j.matpr.2020.11.1023**.

13 N. Mavros, T. Larimian, J. Esqivel, R. K. Gupta, R. Contieri and T. Borkar, *Mater. Des.*, 2019, **183**, 108163, DOI: **10.1016/j.matdes.2019.108163**.

14 M. S. Safavi, F. C. Walsh, L. Visai and J. Khalil-Allafi, *ACS Omega*, 2022, **7**, 9088–9107, DOI: **10.1021/ACSOMEGA.2C00440**.

15 T. C. Senocak, K. V. Ezirmik, F. Aysin, N. Simsek Ozek and S. Cengiz, *Mater. Sci. Eng., C*, 2021, **120**, 111662, DOI: **10.1016/J.MSEC.2020.111662**.

16 B. E. Nagay, J. M. Cordeiro and V. A. R. Barao, in *Alloy Materials and Their Allied Applications*, Scrivener Publishing LLC, 2020, pp. 159–189. DOI: **10.1002/9781119654919.ch9**.

17 G. Mani, D. Porter, K. Grove, S. Collins, A. Ornberg and R. Shulfer, *J. Biomed. Mater. Res., Part A*, 2022, **110**, 1291–1306, DOI: **10.1002/jbm.a.37373**.

18 C. Jimenez-Marcos, J. C. Mirza-Rosca, M. S. Baltatu and P. Vizureanu, *Bioengineering*, 2022, **9**, 686, DOI: **10.3390/bioengineering9110686**.

19 N. A. C. Lah and M. H. Hussin, *Pertani. J. Sci. Technol.*, 2019, **27**, 459–472.

20 S. Ravanbakhsh, C. Paternoster, P. Mengucci, P. Chevallier, S. Gambaro, T. Lescot, C. Paoletti, V. Sales, M. Cabibbo, M. A. Fortin and D. Mantovani, *Mater. Chem. Phys.*, 2023, **297**, 127342, DOI: **10.1016/j.matchemphys.2023.127342**.

21 A. Kumar, M. Mathur, A. K. Sharma, A. Kumar Swami and M. Saran, *Int. J. Pharm. Sci. Res.*, 2020, **11**, 4070, DOI: **10.13040/IJPSR.0975-8232.11(8).4070-77**.

22 N. Bano, S. S. Jikan, H. Basri, S. Adzila, N. A. Badarulzaman, N. N. Ruslan, S. Abdullah and S. H. M. Suhaimy, *Composites in Biomedical Applications*, 2020, pp. 99–116. DOI: 10.1201/9780429327766-5.
23 K. Imai, X. Zhou and X. Liu, *Metals*, 2020, **10**, 203, DOI: 10.3390/met10020203.
24 A. Shahid, B. Aslam, S. Muzammil, N. Aslam, M. Shahid, A. Almatroudi, K. S. Allemailem, M. Saqalein, M. A. Nisar, M. H. Rasool and M. Khurshid, *J. Appl. Biomater. Funct. Mater.*, 2021, **19**, 22808000211040304, DOI: 10.1177/22808000211040304.
25 W. Al-Zyoud, D. Haddadin, S. A. Hasan, H. Jaradat and O. Kanoun, *Materials*, 2023, **16**, 6881, DOI: 10.3390/MA16216881.
26 A. Ak, *ACS Omega*, 2023, **8**, 33802–33808, DOI: 10.1021/ACSOMEGA.3C04252.
27 H. Thissen, A. Koegler, M. Salwiczek, C. D. Easton, Y. Qu, T. Lithgow and R. A. Evans, *NPG Asia Mater.*, 2015, **7**, e225, DOI: 10.1038/am.2015.122.
28 H. I. Moussa, M. Logan, K. Wong, Z. Rao, M. G. Aucoin and T. Y. Tsui, *Micromachines*, 2018, **9**, 464, DOI: 10.3390/mi9090464.
29 B. Groessner-Schreiber, A. Neubert, W. D. Müller, M. Hopp, M. Griepentrog and K. P. Lange, *J. Biomed. Mater. Res., Part A*, 2003, **64**, 591–599, DOI: 10.1002/JBM.A.10417.
30 P. Simon, J. Ihlemann and J. Bonse, *Nanomaterials*, 2021, **11**, 2054, DOI: 10.3390/nano11082054.
31 A. Amelian, K. Wasilewska, D. Megias and K. Winnicka, *Pharmacol. Rep.*, 2017, **69**, 861–870, DOI: 10.1016/J.PHAREP.2017.03.014.
32 R. Nuwayhid, T. Schulz, F. Siemers, J. Schreiter, P. Kobbe, G. Hofmann, S. Langer and O. Kurow, *Biomedicines*, 2024, **12**, 224, DOI: 10.3390/biomedicines12010224.
33 M. Koch and M. K. Włodarczyk-Biegun, *Bioprinting*, 2020, **20**, 2020.03.18.997668, DOI: 10.1101/2020.03.18.997668.
34 M. Benčina, M. Resnik, P. Starič and I. Junkar, *Molecules*, 2021, **26**, 1418, DOI: 10.3390/MOLECULES26051418.
35 J. C. Kade and P. D. Dalton, *Adv. Healthc. Mater.*, 2021, **10**, 2001232, DOI: 10.1002/ADHM.202001232.
36 P. D. Dalton, *Curr. Opin. Biomed. Eng.*, 2017, **2**, 49–57, DOI: 10.1016/j.cobme.2017.05.007.
37 F. Afghah, C. Dikyol, M. Altunbek and B. Koc, *Appl. Sci.*, 2019, **9**, 3540, DOI: 10.3390/APP9173540.
38 M. K. Włodarczyk-Biegun, M. Villiou, M. Koch, C. Muth, P. Wang, J. Ott and A. Del Campo, *ACS Biomater. Sci. Eng.*, 2022, **8**, 3899–3911, DOI: 10.1021/ACSBIOMATERIALS.2C00623.
39 L. A. Bosworth, M. Lanaro, D. A. O'Loughlin, R. A. D'Sa, M. A. Woodruff and R. L. Williams, *Biofabrication*, 2022, **14**, 015015, DOI: 10.1088/1758-5090/ac41a1.
40 P. S. Zieliński, P. K. R. Gudeti, T. Rikmanspoel and M. K. Włodarczyk-Biegun, *Bioact. Mater.*, 2023, **19**, 292–327, DOI: 10.1016/j.bioactmat.2022.04.008.
41 C. Xu, K. Yang, Y. Xu, X. Meng, Y. Zhou, Y. Xu, X. Li, W. Qiao, J. Shi, D. Zhang, J. Wang, W. Xu, H. Yang, Z. Luo and N. Dong, *J. Nanobiotechnol.*, 2024, **22**, 1–18, DOI: 10.1186/S12951-024-02656-5.
42 X. Kong, D. Zhu, Y. Hu, C. Liu, Y. Zhang, Y. Wu, J. Tan, Y. Luo, J. Chen, T. Xu and L. Zhu, *Mater. Des.*, 2024, **238**, 112717, DOI: 10.1016/J.MATDES.2024.112717.
43 S. Homaeigohar and A. R. Boccaccini, *Front. Chem.*, 2022, **9**, 809676, DOI: 10.3389/FCHEM.2021.809676.
44 E. McColl, J. Groll, T. Jungst and P. D. Dalton, *Mater. Des.*, 2018, **155**, 46–58, DOI: 10.1016/J.MATDES.2018.05.036.
45 N. Abbasi, S. Soudi, N. Hayati-Roodbari, M. Dodel and M. Soleimani, *Cell J.*, 2014, **16**, 245–254.
46 M. Sun, X. Sun, Z. Wang, S. Guo, G. Yu and H. Yang, *Polymers*, 2018, **10**, 1290, DOI: 10.3390/POLYM10111290.
47 M. Puertas-Bartolomé, M. K. Włodarczyk-Biegun, A. Del Campo, B. Vázquez-Lasa and J. S. Román, *Polymers*, 2020, **12**, 1–17, DOI: 10.3390/POLYM12091986.
48 U. Posadowska, M. Parizek, E. Filova, M. Wlodarczyk-Biegun, M. Kamperman, L. Bacakova and E. Pamula, *Int. J. Pharm.*, 2015, **485**, 31–40, DOI: 10.1016/J.IJPHARM.2015.03.003.
49 B. J. C. Maxwell Garnett, *Philos. Trans. R. Soc. London, Ser. A*, 1906, **205**, 237–288, DOI: 10.1098/RSTA.1906.0007.
50 S. G. Croll, *Prog. Org. Coat.*, 2020, **148**, 105847, DOI: 10.1016/J.PORGCOAT.2020.105847.
51 K. Fukuda, S. H. N. Lim and A. Anders, *Thin Solid Films*, 2008, **516**, 4546–4552, DOI: 10.1016/J.TSF.2007.05.080.
52 S. Giljean, M. Bigerelle, K. Anselme and H. Haidara, *Appl. Surf. Sci.*, 2011, **257**, 9631–9638, DOI: 10.1016/J.APSUSC.2011.06.088.
53 M. H. Shim, J. Kim and C. H. Park, *Text. Res. J.*, 2014, **84**, 1268–1278, DOI: 10.1177/0040517513495945.
54 M. Ferrari, F. Cirisano and M. Carmen Morán, *Colloids Interfaces*, 2019, **3**, 48, DOI: 10.3390/COLLOIDS3020048.
55 A. Krasowska and K. Sigler, *Front. Cell. Infect. Microbiol.*, 2014, **4**, 112, DOI: 10.3389/FCIMB.2014.00112.
56 M. Krishnakumar, R. Saravanan and V. Narayanan, *J. Bio Tribocorros*, 2020, **6**, 1–11, DOI: 10.1007/S40735-020-00369-4.
57 D. Gong, Y. Zhang, L. Wan, T. Qiu, Y. Chen and S. Ren, *Process Saf. Environ. Prot.*, 2022, **159**, 708–715, DOI: 10.1016/J.PSEP.2022.01.029.
58 R. N. Ghosh, J. Thomas, B. R. Vaidehi, N. G. Devi, A. Janardanan, P. K. Namboothiri and M. Peter, *Mater. Adv.*, 2023, **4**, 5496–5529, DOI: 10.1039/D3MA00715D.
59 M. Shahverdi, S. Seifi, A. Akbari, K. Mohammadi, A. Shamloo and M. R. Movahhedy, *Sci. Rep.*, 2022, **12**, 1–16, DOI: 10.1038/s41598-022-24275-6.
60 P. G. Saiz, A. Reizabal, J. L. Vilas-Vilela, P. D. Dalton and S. Lanceros-Mendez, *Adv. Mater.*, 2024, **36**, 2312084, DOI: 10.1002/ADMA.202312084.
61 X. Wu, T. Vedelaar, R. Li, R. Schirhagl, M. Kamperman and M. K. Włodarczyk-Biegun, *Bioprinting*, 2023, **32**, e00288, DOI: 10.1016/J.BPRINT.2023.E00288.
62 B. Lv, L. Lu, L. Hu, P. Cheng, Y. Hu, X. Xie, G. Dai, B. Mi, X. Liu and G. Liu, *Theranostics*, 2023, **13**, 2015–2039, DOI: 10.7150/THNO.80615.
63 X. Zhou, Y. Pan, R. Liu, X. Luo, X. Zeng, D. Zhi, J. Li, Q. Cheng, Z. Huang, H. Zhang and K. Wang, *J. Bioact. Compat. Polym.*, 2019, **34**, 115–130, DOI: 10.1177/0883911519835569.

64 D. Jeong, C. Han, I. Kang, H. T. Park, J. Kim, H. Ryu, Y. S. Gho and J. Park, *PLoS One*, 2016, **11**, e0148846, DOI: **10.1371/JOURNAL.PONE.0148846**.
65 A. Merivaara, E. Koivunotko, K. Manninen, T. Kaseva, J. Monola, E. Salli, R. Koivuniemi, S. Savolainen, S. Valkonen and M. Yliperttula, *Polymers*, 2022, **14**, 5530, DOI: **10.3390/polym14245530**.
66 K. Duval, H. Grover, L. H. Han, Y. Mou, A. F. Pegoraro, J. Fredberg and Z. Chen, *Physiology*, 2017, **32**, 266–277, DOI: **10.1152/PHYSIOL.00036.2016**.
67 X. Cui, Y. Hartanto and H. Zhang, *J. R. Soc. Interface*, 2017, **14**, 20160877.
68 T. L. Jenkins and D. Little, *npj Regener. Med.*, 2019, **4**, 1–14, DOI: **10.1038/s41536-019-0076-5**.
69 M. S. Brescó, L. G. Harris, K. Thompson, B. Stanic, M. Morgenstern, L. O'Mahony, R. G. Richards and T. F. Moriarty, *Front. Microbiol.*, 2017, **8**, 1401, DOI: **10.3389/FMICB.2017.01401**.
70 E. Zhang, X. Zhao, J. Hu, R. Wang, S. Fu and G. Qin, *Bioact. Mater.*, 2021, **6**, 2569–2612, DOI: **10.1016/J.BIOACTMAT.2021.01.030**.